

Reconstructing ultrafast energy-time entangled two-photon pulses

Jean-Philippe W. MacLean,^{1,2,*} Sacha Schwarz,^{1,2,†} and Kevin J. Resch^{1,2}

¹*Institute for Quantum Computing, University of Waterloo, Waterloo, Ontario, Canada, N2L 3G1*

²*Department of Physics & Astronomy, University of Waterloo, Waterloo, Ontario, Canada, N2L 3G1*

The generation of ultrafast laser pulses and the reconstruction of their electric fields is essential for many applications in modern optics. Quantum optical fields can also be generated on ultrafast time scales, however, the tools and methods available for strong laser pulses are not appropriate for measuring the properties of weak, possibly entangled pulses. Here, we demonstrate a method to reconstruct the joint-spectral amplitude of a two-photon energy-time entangled state from joint measurements of the frequencies and arrival times of the photons, and the correlations between them. Our reconstruction method is based on a modified Gerchberg-Saxton algorithm. Such techniques are essential to measure and control the shape of ultrafast entangled photon pulses.

I. INTRODUCTION

The generation, control, and measurement of high-dimensional entangled quantum states of light are important for optical computing and communication [1–4]. One form of this entanglement, in the energy-time degree of freedom, can exhibit strong correlations in frequency and time [5, 6], nonlocal interference phenomena [7, 8], and dispersion cancellation [9, 10], with applications in high-capacity quantum key distribution [11, 12], enhanced spectroscopy [13], sensing [14], and two-photon absorption [15]. The generation and control of energy-time entanglement has been realized in both bulk crystals and waveguide structures [16–20], however, it remains an important challenge to reconstruct the quantum state of the photons produced. The performance of any quantum optical technology using time and frequency depends on being able to both shape and completely characterize such photonic states.

In ultrafast optics and laser physics, the ability to measure the amplitude and phase of laser pulses on ultrafast timescales is essential for nonlinear optics and spectroscopy. In this context, the problem of electric field reconstruction has been extensively studied [21]. Optical pulses can be produced on time scales much shorter than any photodetector response time [22], and consequently, the only thing fast enough to measure an ultrafast laser pulse is another ultrafast pulse. Techniques such as FROG [23] and SPIDER [24] make use of nonlinear optical processes to measure and reconstruct ultrafast pulses. However, adapting them to quantum states of light is challenging due to the low power levels of single photons. In addition, the algorithms developed for laser pulses do not account for the possibility that photons can be entangled. New innovations are therefore needed to reconstruct the joint state of entangled ultrafast photon pulses.

Approaches for characterizing the optical modes of photons have been explored using homodyne measure-

ments [25–30], two-photon interference effects [31–33], and two-photon absorption in semiconductors [34]. The increased interest in time-frequency modes has also led to nonlinear ultrafast approaches for characterization [35–38]. To measure both the frequency and time intensity correlations of energy-time entangled states, optical methods based on optical gating and frequency resolved measurements have recently been developed. These have been used to observe nonlocal dispersion cancellation [39] and two-photon quantum interferometry [40] on time scales inaccessible to standard photodetectors. For complete characterization, however, the joint spectral phase is also required. This additional phase information is important to understand the nature of the entanglement and to control and optimize the performance of quantum information protocols using heralded and multi-photon states [41].

Recovering the phase of a field from intensity measurements in Fourier-related domains is known as a phase-retrieval problem. In 1972, Gerchberg and Saxton provided a practical solution to this problem. They introduced an iterative algorithm, referred to as the Gerchberg-Saxton algorithm (GS), to extract the complete wavefunction of an electron beam, including its phase, from intensity recordings in the image and diffraction planes [42]. Their algorithm can be applied to problems involving electromagnetic waves [43, 44] including optical wavelengths [45].

In this paper, we implement a technique to recover the phase of ultrafast energy-time entangled two-photon pulses produced via spontaneous parametric downconversion (SPDC) and which is based on intensity measurements of the frequency and the arrival time of the photons. Inspired by the conventional phase retrieval problem, we develop an algorithm based on a method of alternate projections [42, 46, 47] that iterates between the frequency and time domains imposing the measured intensity constraints at each iteration. Measurements in frequency are performed with single-photon spectrometers and measurements in time are implemented via optical gating with an ultrafast optical laser pulse.

* jpmaclean@uwaterloo.ca

† sacha.schwarz@uwaterloo.ca

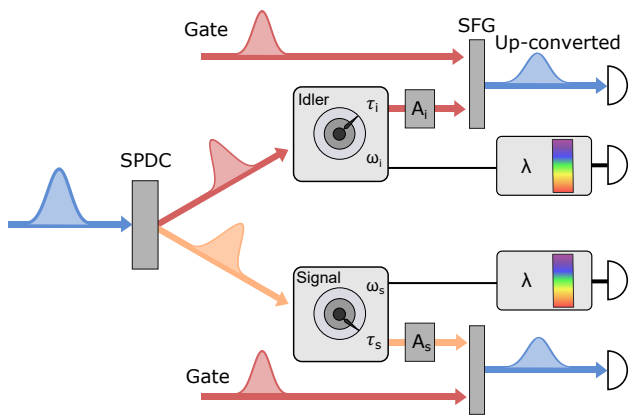


FIG. 2. Experimental setup for two-photon state reconstruction. Energy-time entangled photons are produced through spontaneous parametric downconversion (SPDC). Each photon can be measured in frequency using a scanning monochromator or in time by optically gating the single photon using sum-frequency generation (SFG) in a nonlinear medium with a strong gate pulse. The delays τ_s and τ_i are between the gate pulse and the photon on the signal and idler side, respectively. The quadratic spectral phases, A_s on the signal photon and A_i on the idler photon, are controlled using a fibre and grating compressor on each side. Measurements in coincidence of all four combinations of the frequency and time of arrival of the photons allow the reconstruction of the joint spectral amplitude function using a phase retrieval algorithm.

pulses [80 MHz, 775 nm, 3.8 W average power, 0.130 ps (s.d.) pulse width], are frequency doubled in 2 mm of β -bismuth borate (BiBO). After spectral filtering with a 0.2 nm FWHM bandpass filter, the second harmonic pumps a 5 mm BiBO crystal for type-I SPDC generating energy-time entangled photons at 823 nm and 732 nm. These are coupled in single-mode fibres allowing for direct, spectrally resolved, or temporally resolved measurements. Spectral measurement are performed via monochromators with a resolution of 0.1 nm. Temporal measurements are implemented via optical gating, i.e., via noncollinear sum-frequency generation (SFG) with femtosecond laser pulses in 1 mm of bismuth borate (BiBO) crystal. The electric field of the gate pulse is characterized using an SHG-FROG measurement, and we find an intensity pulse width of 130 fs (s.d.). Since the experimentally measured intensity in frequency (time) is convolution of the joint spectral (temporal) intensity and the filter function of the monochromator (temporal gate), the measured data must first be deconvolved before it can be used in the phase-retrieval algorithm. Numerical deconvolutions for each intensity measurement are performed using a Wiener filter [54], and the resulting output provides the intensity distributions, $I(\omega_s, \omega_i)$, $I(t_s, \omega_i)$, $I(\omega_s, t_i)$, $I(t_s, t_i)$, used in the algorithm in Fig. 1. See Appendix A for further details.

The spectral phase on the photons,

$$\phi(\omega_s, \omega_i) \approx A_s (\omega_s - \omega_{s0})^2 + A_i (\omega_i - \omega_{i0})^2, \quad (7)$$

is controlled with a combination of normally dispersive single-mode fibre and adjustable grating compressor for anomalous dispersion [39], where A_s and A_i are the chirp parameters for the signal and idler, respectively. The relative position of the gratings inside the compressor sets the magnitude and sign of the overall dispersion. We calibrate both grating compressors using XFROG (Cross-correlation FROG) spectrogram measurements between the strong gate pulse and a weak laser pulse. The weak laser pulse has the same center wavelength and path through the fibre-compressor system as the photons on each side. The phase at each relative grating separation is reconstructed using the Principal Component Generalized Projection (PCGP) FROG algorithm [52, 55]. We find a quadratic phase that depends linearly on the grating separation with slopes of $(-1360 \pm 60) \text{ fs}^2/\text{mm}$ and $(-2190 \pm 70) \text{ fs}^2/\text{mm}$ for the signal and idler, respectively. The difference between the two is attributed to the cubic dependence on wavelength of dispersion in a grating compressor [56].

V. PHASE RECONSTRUCTIONS

We compare the phase retrieval algorithm on measured data for two-photon states with different amounts of dispersion. We set the grating compressors on the signal and idler side to study four cases: no additional dispersion, with extra positive dispersion applied to the idler, with extra negative dispersion applied to the signal, and with extra negative dispersion applied on both sides. For the case of a two-photon energy-time entangled state with negative dispersion applied to both photons, an example of the four combinations of time and frequency measurements is shown in Fig. 3. Background subtraction, a Wiener Filter, and low-pass filters are applied in Fig. 3 and prior to the reconstruction [57]. We observe strong anti-correlations in the joint spectral intensity [Fig. 3(a)], however, the joint temporal intensity [Fig. 3(d)] is uncorrelated due to the presence of dispersion on both photons. The observed shears in both the time-frequency intensity plots [Fig. 3(b-c)] also illustrate the presence of negative dispersion.

We map these intensity constraints onto a 64x64 array and input them into the phase retrieval algorithm, which is run for 1000 iterations, a number found heuristically after which no reduction in the FROG-trace error is observed. The intensity of the reconstructed wavefunction in frequency and time are shown in Fig. 4. The reconstructed intensities are compared to the measured data from Fig. 3(a) and Fig. 3(d). We find a FROG-trace error between the post-processed and reconstructed spectral intensities after 1000 iterations to be $(3.64 \pm 0.07)\%$ for the joint spectral intensity and $(7.01 \pm 0.35)\%$ for the joint temporal intensity.

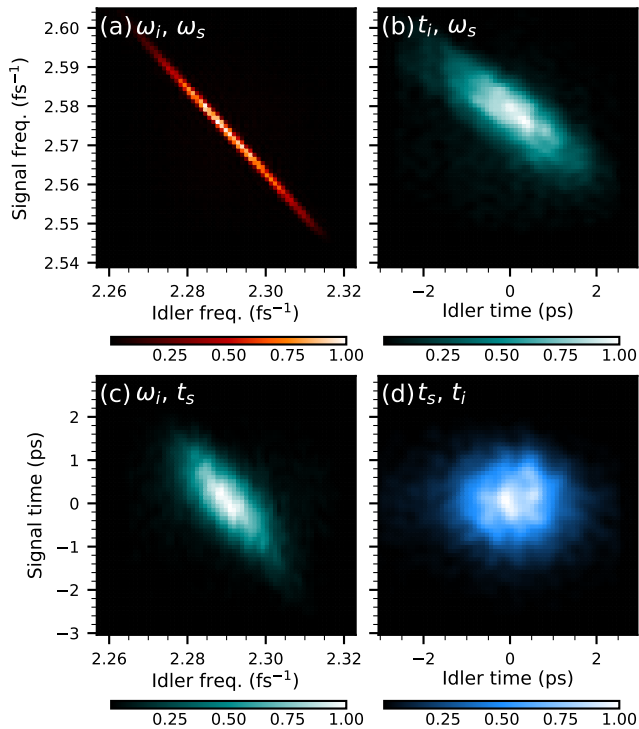


FIG. 3. Example deconvolved measured data for two-photon state reconstruction when negative dispersion is introduced to signal and idler photons. Combinations of spectral and temporal measurements are made in coincidence to obtain the (a) joint spectral intensity, (d) joint temporal intensity, and (b,c) correlations between the time and frequency of the photon pair for an SPDC state. We observe strong anti-correlations between the measured quantities in (a), (b), (c) and very little correlations in (d), indicating the presence of negative dispersion on both photons. After post-processing, the measured intensities are used as data constraints for the phase-retrieval algorithm.

Note that the marginal bandwidths of the joint spectral intensity in the reconstruction [Fig. 4(a)] are shorter than in the original data [Fig. 3(a)]. Numerical simulations suggest that this arises as a result of the phase-matching bandwidth in the optical gating. The effect of the phase mismatch on the reconstruction of two-photon states with optical gating is modelled in Appendix B.

Fig. 5 shows the reconstructed joint spectral phase for the four different cases. Starting with the case where we attempted to minimize the unbalanced dispersion [Fig. 5(a)], we observe a relatively flat spectral phase. In this configuration, we measure the time-bandwidth product as in Ref. [39] and find $\Delta(\omega_s + \omega_i)\Delta(t_s - t_i) = (1.711 \pm 0.005)(0.196 \pm 0.004) = 0.348 \pm 0.006$, verifying the presence of energy-time entanglement.

For the three cases where dispersion is applied, we fit the reconstructed quadratic spectral phase in Fig. 5(b-d). For each, we unwrap the 2D phase and perform a polynomial fit to the phase distribution. The corresponding

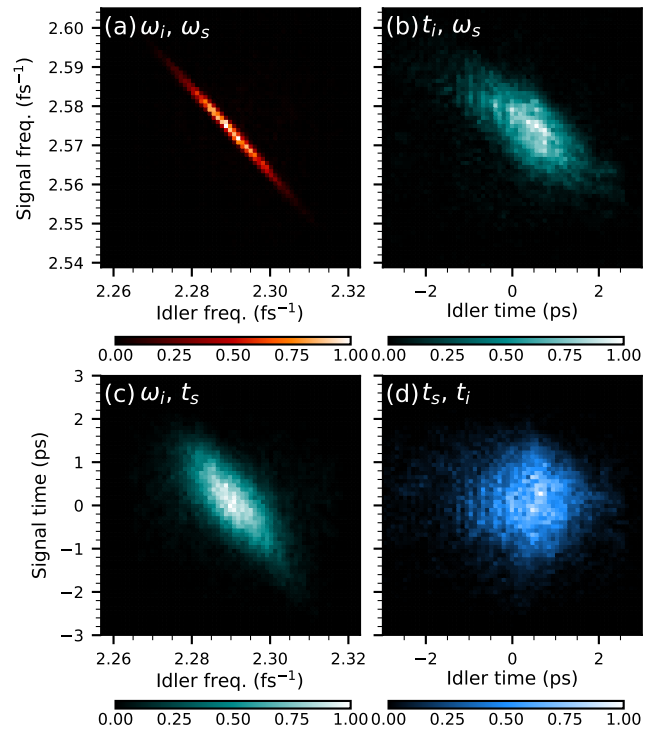


FIG. 4. Two-photon state reconstruction. Reconstructed distributions for the (a) the joint spectral intensity, (d) the joint temporal intensity, as well the (b,c) time-frequency correlations of the measured state in Fig. 3 after 1000 iterations of the phase retrieval algorithm.

uncertainties are obtained from the variance in the fitted spectral phase after performing Monte Carlo simulations assuming Poissonian noise.

When we apply $A_s = (0.026 \pm 0.002) \text{ ps}^2$ of dispersion on the signal photon [Fig. 5(b)], we reconstruct a quadratic spectral phase on the signal of $A_s = (0.024 \pm 0.003) \text{ ps}^2$, observing a positive quadratic variation in the phase along the signal (y) axis, modulo 2π , with little variations along the idler (x) axis. When we apply $A_i = (-0.025 \pm 0.002) \text{ ps}^2$ of dispersion to the idler photon [Fig. 5(c)], we reconstruct a quadratic phase on the idler of $A_i = (-0.026 \pm 0.003) \text{ ps}^2$, observing a negative quadratic variation in the spectral phase along the idler (x) axis, with again little variations along the signal (y) axis. When we apply $A_s = (-0.036 \pm 0.004) \text{ ps}^2$ and $A_i = (-0.043 \pm 0.002) \text{ ps}^2$ of dispersion to the signal and idler [Fig. 5(d)], we reconstruct a quadratic phase on the signal and idler of $A_s = (-0.036 \pm 0.004) \text{ ps}^2$ and $A_i = (-0.028 \pm 0.003) \text{ ps}^2$, respectively. For this case, we observe a negative quadratic variation along the diagonal x-y axis.

When dispersion is applied to only one photon, Fig. 5(b) and Fig. 5(c), the phase obtained using the phase-retrieval algorithm corresponds to the reconstructed phases measured using the XFROG algorithm.

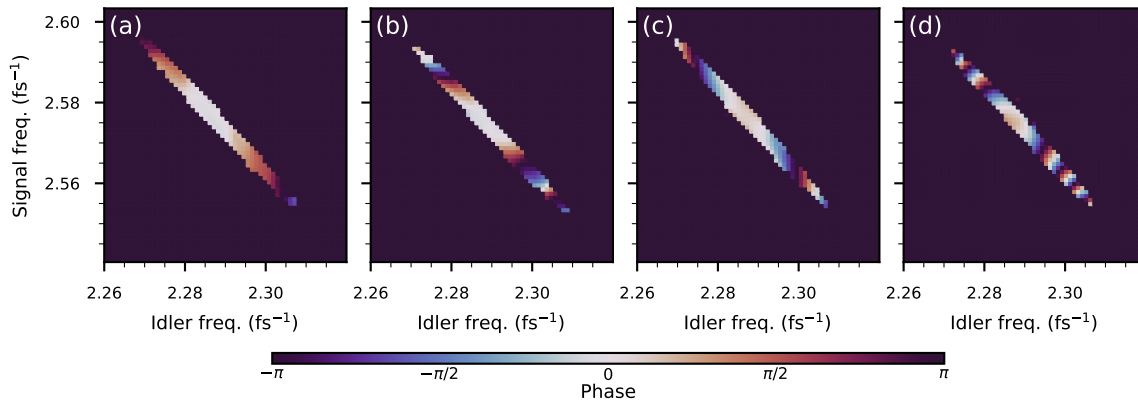


FIG. 5. Phase reconstruction of energy-time entangled states. Reconstructed joint spectral phase for energy-time entangled photon pairs with (a) no added dispersion, (b) positive dispersion on the signal, (c) negative dispersion on the idler, (d) negative dispersion on both the signal and idler. Phase points outside the 2σ intensity contours are removed for clarity. We observe (a) a relatively flat phase variation, (b) a positive quadratic phase variation along the signal axis, (c) a negative quadratic phase variation along the idler axis, (d) and a negative quadratic phase variation along both axes.

In the last case, Fig. 5(d), we find a discrepancy between the two. This, again, is likely due to the effect of the phase mismatch on the temporal measurements and on the subsequent reconstruction of two-photon states, which will be more pronounced for the photons which have much larger bandwidth than for the weak pulse used for the XFROG reconstructions (see Appendix B).

VI. CONCLUSION

We have demonstrated a method to recover ultrafast two-photon energy-time entangled pulses. Our technique is based on a method of alternate projections that iterates between the frequency and time domains imposing the measured intensity constraints at each iteration. The use of nonlinear phenomena, i.e., optical gating, to measure the timing correlations is an artifact of the time scales at play and is not a fundamental requirement. For sufficiently long pulses, there may exist photodetectors that can measure the temporal intensity directly [58]. For sub-picosecond resolution involving optical gating, the effect of phase-matching in the upconversion could be reduced using shorter crystals or angle-dithering [59].

In our simulations, the reconstruction fidelity seems to depend on the amount of entanglement in the initial state, and uncovering the reason for this is the subject of future work. Moreover, extensions of this algorithm to characterize two-photon mixed states may be possible based on techniques used to reconstruct partially coherent light [60, 61], removing assumptions about the purity of the quantum states. Measurement and reconstruction capabilities similar to those available in ultrafast optics will be essential for developing new applications in quantum state engineering and ultrafast shaping of entangled photons, paving the way to characterizing and manipu-

lating high-dimensional quantum states of light.

The authors thank J.M. Donohue and F. Miatto for fruitful discussions. This research was supported in part by the Natural Sciences and Engineering Research Council of Canada (NSERC), Canada Research Chairs, Industry Canada and the Canada Foundation for Innovation (CFI).

Appendix A: Phase retrieval algorithm

The algorithm to reconstruct the phase of energy-time entangled states is divided into two main parts: post-processing and phase retrieval. In the first part, post-processing, for each experimentally measured time-frequency correlation plot, the data is interpolated onto a 2D square grid, $H(x, y)$, of size 64×64 , where, here, we use x, y to represent either the measured time or frequency variables. We apply background subtraction using a corner suppression routine [52]. The numerical deconvolution is performed using a Wiener filter,

$$W(k_x, k_y) = \frac{G(k_x, k_y)^*}{|G(k_x, k_y)|^2 + \alpha}, \quad (\text{A1})$$

where $G(k_x, k_y)$ is the filter function which we obtain by taking the Fourier transform of the instrument response functions. These are approximated as Gaussian functions with the instrument resolutions obtained experimentally for the spectral (0.1 nm) and temporal (0.130 ps) measurements. The parameter α takes into account the amount of noise in the system and will typically depend on k_x and k_y . Here, we approximate it as a constant, $0.05 \leq \alpha \leq 0.2$, which is obtained heuristically for each reconstruction. A low-pass filter is also applied by multiplying the Wiener filter $W(k_x, k_y)$ by a top-hat function

$T(k_x, k_y)$ of radius, $\varrho N/2$ in pixels, and setting all the values outside $\varrho N/2$ to 0, where N is the size of the grid, and $0.8 \leq \varrho \leq 1$. The deconvolved intensities are then obtained with the inverse Fourier transform,

$$I(x, y) = FT^{-1} [H(k_x, k_y)W(k_x, k_y)T(k_x, k_y)], \quad (\text{A2})$$

where $H(k_x, k_y)$ is the Fourier Transform of the experimentally measured intensities $H(x, y)$. The resulting deconvolved intensities $I(x, y)$ are used as the physical constraints in the phase retrieval algorithm.

In the second part, the phase retrieval algorithm is seeded with an initial guess of the state, which can consist of the measured amplitudes with a random phase. Steps (1-8) are used when all four intensity constraints are applied.

1. Replace the magnitude of $F_{\omega\omega}(\omega_s, \omega_i)$ with the measured values

$$F'_{\omega\omega}(\omega_s, \omega_i) = \frac{F_{\omega\omega}(\omega_s, \omega_i)}{|F_{\omega\omega}(\omega_s, \omega_i)|} \sqrt{I(\omega_s, \omega_i)}. \quad (\text{A3})$$

2. Evaluate the inverse Fourier transform $F_{\omega\omega}(\omega_s, \omega_i)$ to obtain an estimate of $F_{\omega t}(\omega_s, t_i)$.

3. Replace the magnitude of $F_{\omega t}(\omega_s, t_i)$ with the measured values

$$F'_{\omega t}(\omega_s, t_i) = \frac{F_{\omega t}(\omega_s, t_i)}{|F_{\omega t}(\omega_s, t_i)|} \sqrt{I(\omega_s, t_i)}. \quad (\text{A4})$$

4. Evaluate the inverse Fourier transform $F'_{\omega t}(\omega_s, t_i)$ to obtain an estimate of $F_{tt}(t_s, t_i)$.

5. Replace the magnitude of $F_{tt}(t_s, t_i)$ with the measured values

$$F'_{tt}(t_s, t_i) = \frac{F_{tt}(t_s, t_i)}{|F_{tt}(t_s, t_i)|} \sqrt{I(t_s, t_i)}. \quad (\text{A5})$$

6. Evaluate the Fourier transform $F'_{tt}(t_s, t_i)$ to obtain an estimate of $F_{t\omega}(t_s, \omega_i)$.

7. Replace the magnitude of $F_{t\omega}(t_s, \omega_i)$ with the measured values

$$F'_{t\omega}(t_s, \omega_i) = \frac{F_{t\omega}(t_s, \omega_i)}{|F_{t\omega}(t_s, \omega_i)|} \sqrt{I(t_s, \omega_i)}. \quad (\text{A6})$$

8. Evaluate the Fourier transform $F'_{t\omega}(t_s, \omega_i)$ to obtain an estimate of $F_{\omega\omega}(\omega_s, \omega_i)$.

The time to run the algorithm depends on the size of the arrays being used and the number of iterations. For the case in Fig. 4, using a 64x64 array, the entire procedure, including loading the data, applying filtering and deconvolution algorithms, and running the phase retrieval algorithm for 1000 iterations takes about (10 ± 4) s, averaged over 100 runs and using a laptop computer (i7-4650U CPU @2.3GHz with 8 Gb of RAM).

Appendix B: Reconstructing two-photon states with optical gating

To test the numerical deconvolution and the phase-reconstruction algorithm described above using realistic temporal measurements, we construct a numerical model of optical gating with thick crystals and consider its effect on the measurement and reconstruction of energy-time entangled two-photon states.

An energy-time entangled two-photon state as in Eq. 1 with a joint-spectral amplitude for the signal ω_s and idler ω_i frequencies is modelled with a two-dimensional correlated Gaussian function,

$$F_{\omega\omega}(\omega_s, \omega_i) = \frac{1}{\sqrt{2\pi}\sigma_{\omega_s}\sigma_{\omega_i}(1-\rho_\omega^2)^{1/4}} \exp\left(-\frac{1}{2(1-\rho_\omega^2)}\left[\frac{(\omega_s - \omega_{s0})^2}{2\sigma_{\omega_s}^2} + \frac{(\omega_i - \omega_{i0})^2}{2\sigma_{\omega_i}^2} - \frac{\rho_\omega(\omega_s - \omega_{s0})(\omega_i - \omega_{i0})}{\sigma_{\omega_s}\sigma_{\omega_i}}\right]\right). \quad (\text{B1})$$

The marginal frequency bandwidths, σ_{ω_i} and σ_{ω_s} , are set to the values measured experimentally. The correlation parameter $\rho_\omega = \Delta(\omega_s\omega_i)/\Delta\omega_s\Delta\omega_i$ describes the statistical correlations between the frequency of the signal and idler modes and is related to the purity of the partial trace, $P = \sqrt{1-\rho_\omega^2}$. When $\rho_\omega = 0$, the joint-spectral amplitude $F(\omega_s, \omega_i)$ factorizes and the state is

separable, whereas when $\rho_\omega \rightarrow -1$, the photons are perfectly anticorrelated in frequency. Furthermore, when the marginal bandwidths are equal, $\sigma_{\omega_s} = \sigma_{\omega_i}$, the time-bandwidth product for the Gaussian state in Eq. B1 is $\Delta(\omega_s + \omega_i)\Delta(t_s - t_i) = \sqrt{(1+\rho)/(1-\rho)}$. We apply a

quadratic phase to the state,

$$F_{\omega\omega}(\omega_s, \omega_i) \rightarrow F_{\omega\omega}(\omega_s, \omega_i) e^{iA_s(\omega_s - \omega_{s0})^2 + iA_i(\omega_i - \omega_{i0})^2}, \quad (\text{B2})$$

where A_s and A_i are the chirp parameters on the signal and idler, respectively.

In the SFG process used for optical gating, a photon and a strong gate pulse in the near-infrared (NIR) are up-converted to produce a higher energy photon in the ultraviolet. If the photons are dispersed before the optical gating, high and low frequencies components will arrive at different times in the nonlinear medium. In the presence of phase mismatch, the upconverted frequencies associated to these high and low frequency components can lie outside the phase-matching bandwidth of the crystal, and consequently will be suppressed. As a result, phase mismatch in optical gating changes the measured intensity correlations and therefore changes the deconvolved intensity constraints that are applied in the phase retrieval algorithm.

To account for this effect, we model the optical gating as sum-frequency generation process in the low-efficiency regime between the photons on each side and a gate pulse with centre frequency ω_g and a pulse duration of 0.130 ps, leading to upconverted frequencies $\omega_{u_s} = \omega_s + \omega_g$ and $\omega_{u_i} = \omega_i + \omega_g$ on the signal and idler side, respectively. The gate pulse is modeled with a Gaussian temporal profile,

$$G(\omega_g, \tau_g) = \frac{1}{(2\pi\sigma_g^2)^{\frac{1}{4}}} e^{-\frac{(\omega_g - \omega_{g0})^2}{4\sigma_g^2} + i\tau_g(\omega_g - \omega_{g0})}, \quad (\text{B3})$$

with marginal bandwidth σ_g , and delay τ_g . For the purpose of this simulation, we assume the spectral measurements have high resolution such that they can be represented by delta functions,

$$H_{\omega\omega}(\omega_s, \omega_i) \approx |F(\omega_s, \omega_i)|^2, \quad (\text{B4})$$

and the three intensity measurements involving optical gating are calculated via the following,

$$H_{\tau\omega}(\tau_s, \omega_i) = \int d\omega_{u_s} \left| \int d\omega_s G(\omega_{u_s} - \omega_s, \tau_s) \Phi_{\text{SFG}}(\omega_s, \omega_{u_s} - \omega_s, \omega_{u_s}) F_{\omega\omega}(\omega_s, \omega_i) \right|^2, \quad (\text{B5})$$

$$H_{\omega\tau}(\omega_s, \tau_i) = \int d\omega_{u_i} \left| \int d\omega_i G(\omega_{u_i} - \omega_i, \tau_i) \Phi_{\text{SFG}}(\omega_i, \omega_{u_i} - \omega_i, \omega_{u_i}) F_{\omega\omega}(\omega_s, \omega_i) \right|^2, \quad (\text{B6})$$

$$H_{\tau\tau}(\tau_s, \tau_i) = \int d\omega_{u_s} d\omega_{u_i} \left| \int d\omega_s d\omega_i G(\omega_{u_s} - \omega_s, \tau_s) \Phi_{\text{SFG}}(\omega_s, \omega_{u_s} - \omega_s, \omega_{u_s}) \right. \\ \left. \times G(\omega_{u_i} - \omega_i, \tau_i) \Phi_{\text{SFG}}(\omega_i, \omega_{u_i} - \omega_i, \omega_{u_i}) F_{\omega\omega}(\omega_s, \omega_i) \right|^2, \quad (\text{B7})$$

where the gate pulse G is the same on both sides but with delays τ_i and τ_s introduced. The phase matching function is

$$\Phi_{\text{SFG}}(\omega_j, \omega_{u_j} - \omega_j, \omega_{u_j}) = e^{-i\frac{\Delta k L}{2}} \text{sinc}\left(\frac{\Delta k L}{2}\right), \quad (\text{B8})$$

where the phase-mismatch,

$$\Delta k(\omega_j, \omega_{u_j} - \omega_j, \omega_{u_j}) = \frac{n_e(\omega_j)\omega_j}{c} + \frac{n_o(\omega_{u_j})\omega_{u_j}}{c} \\ + \frac{n_e(\omega_{u_j} - \omega_j)(\omega_{u_j} - \omega_j)}{c}, \quad (\text{B9})$$

is calculated for type-I SFG with different crystal lengths L and the experimentally measured wavelengths. The phase-matching bandwidth can be estimated from the range of frequencies contained in $\Delta k L = \pi$. Upconverted frequencies outside this range are suppressed. All integrals are evaluated numerically.

We model all the steps in the phase-retrieval process. We numerically create frequency anti-correlated states using Eq. B1 and Eq. B2, with the same centre wavelength and bandwidth as those measured experimentally, but with different amounts of applied spectral phases, given by the chirp parameters A_s and A_i . We calculate the four joint correlations in frequency and time with Eqs. (B4-B7) using different lengths of BiBO for optical gating, apply the numerical deconvolution to each intensity measurement as described in Appendix A, and insert these as constraints for the phase retrieval algorithm. After reconstruction, we unwrap the spectral phase of the reconstructed joint spectral amplitude function and fit it to a third-order two-dimensional polynomial.

The reconstructed spectral phases are compared to the applied spectral phases in Fig. 6 for different lengths of BiBO used in optical gating and for different applied spectral phases. In Fig. 6(a) and Fig. 6(b), the signal chirp parameter A_s is kept fixed while the idler chirp parameter is varied, whereas in Fig. 6(c) and Fig. 6(d),

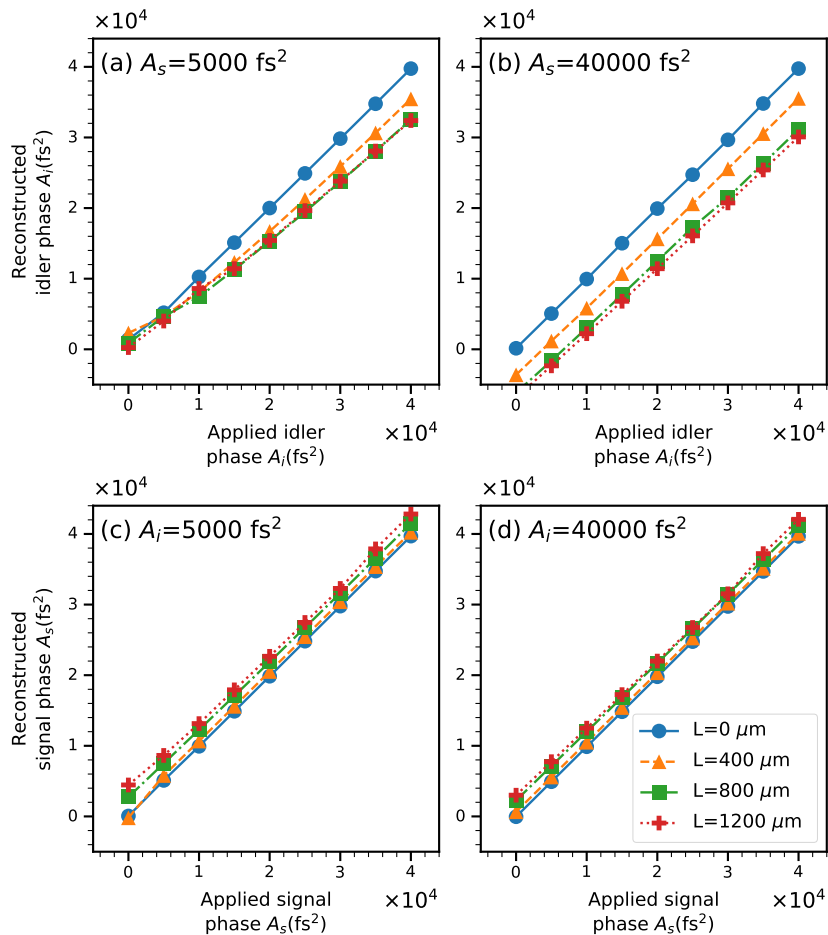


FIG. 6. Effect of phase mismatch on the reconstructed spectral phase. We model the effect of optical gating with different lengths L of BiBO on the reconstructed phase. The reconstructed phase is compared to the applied phase for four different cases. The signal chirp parameter is fixed to the values of (a) $A_s = 5,000 \text{ fs}^2$ and (b) $A_s = 40,000 \text{ fs}^2$ while the idler chirp parameter A_i is varied. The idler chirp parameter is fixed to the values of (c) $A_i = 5,000 \text{ fs}^2$ and (d) $A_i = 40,000 \text{ fs}^2$ while the signal chirp parameter A_s is varied. At $L = 0 \mu\text{m}$, the reconstructed phase is the same as the applied phase. As L is increased, phase mismatch becomes more important and this changes the value of the reconstructed phase.

the idler chirp parameter A_i is kept fixed while the signal chirp parameter A_s is varied. When the length of the crystal is set to zero ($L = 0 \mu\text{m}$), the reconstructed phase corresponds exactly to the applied phase, and the line at $L = 0 \mu\text{m}$ appears at 45 degrees with a slope of one. As the length of the crystal increases, we find that the slope remains fairly constant at 45 degrees, but the offset

depends on the configuration. For example, comparing Fig. 6(a) and Fig. 6(b), we find the values of the reconstructed idler chirp parameter A_i depend on whether the signal chirp parameter has a value of $A_s = 5,000 \text{ fs}^2$ [Fig. 6(a)] or $A_s = 40,000 \text{ fs}^2$ [Fig. 6(b)]. The difference between the reconstructed and applied phase in Fig. 6 also becomes larger for longer crystals where the phase matching function is more restrictive.

-
- [1] B. P. Lanyon, M. Barbieri, M. P. Almeida, T. Jennewein, T. C. Ralph, K. J. Resch, G. J. Pryde, J. L. O'Brien, A. Gilchrist, and A. G. White, *Nat. Phys.* **5**, 134 (2009).
- [2] M. Kues, C. Reimer, P. Roztocky, L. R. Cortés, S. Sciara, B. Wetzal, Y. Zhang, A. Cino, S. T. Chu, B. E. Little, D. J. Moss, L. Caspani, J. Azaña, and R. Morandotti, *Nature* **546**, 622 (2017).
- [3] Y. Cai, J. Roslund, G. Ferrini, F. Arzani, X. Xu, C. Fabre, and N. Treps, *Nat. Commun.* **8**, 15645 (2017).
- [4] C. Sparrow, E. Martín-López, N. Maraviglia, A. Neville, C. Harrold, J. Carolan, Y. N. Joglekar, T. Hashimoto, N. Matsuda, J. L. O'Brien, D. P. Tew, and A. Laing, *Nature* **557**, 660 (2018).
- [5] P. van Loock and A. Furusawa, *Phys. Rev. A* **67**, 052315

- (2003).
- [6] L. K. Shalm, D. R. Hamel, Z. Yan, C. Simon, K. J. Resch, and T. Jennewein, *Nat. Phys.* **9**, 19 (2013).
- [7] J. D. Franson, *Phys. Rev. Lett.* **62**, 2205 (1989).
- [8] P. G. Kwiat, A. M. Steinberg, and R. Y. Chiao, *Phys. Rev. A* **47**, R2472 (1993).
- [9] J. D. Franson, *Phys. Rev. A* **45**, 3126 (1992).
- [10] T. Wasak, P. Szankowski, W. Wasilewski, and K. Banaszek, *Phys. Rev. A* **82**, 052120 (2010).
- [11] J. Nunn, L. J. Wright, C. Söller, L. Zhang, I. A. Walmsley, and B. J. Smith, *Opt. Express* **21**, 15959 (2013).
- [12] T. Zhong, H. Zhou, R. D. Horansky, C. Lee, V. B. Verma, A. E. Lita, Alessandro Restelli, J. C. Bienfang, R. P. Mirin, T. Gerrits, S. W. Nam, F. Marsili, M. D. Shaw, Z. Zhang, L. Wang, D. Englund, G. W. Wornell, J. H. Shapiro, and F. N. C. Wong, *New J. Phys.* **17**, 022002 (2015).
- [13] M. G. Raymer, A. H. Marcus, J. R. Widom, and D. L. P. Vitullo, *J. Phys. Chem. B* **117**, 15559 (2013).
- [14] Z. Zhang, S. Mouradian, F. N. C. Wong, and J. H. Shapiro, *Phys. Rev. Lett.* **114**, 110506 (2015).
- [15] B. Dayan, A. Pe'er, A. A. Friesem, and Y. Silberberg, *Phys. Rev. Lett.* **93**, 023005 (2004).
- [16] D. Kang, A. Pang, Y. Zhao, and A. S. Helmy, *J. Opt. Soc. Am. B* **31**, 1581 (2014).
- [17] J. M. Donohue, M. Mastrovich, and K. J. Resch, *Phys. Rev. Lett.* **117**, 243602 (2016).
- [18] J. M. Donohue, V. Ansari, J. Řeháček, Z. Hradil, B. Stoklasa, M. Paúr, L. L. Sánchez-Soto, and C. Silberhorn, *arXiv:1805.02491* (2018), *arXiv: 1805.02491*.
- [19] F. Arzani, C. Fabre, and N. Treps, *Phys. Rev. A* **97**, 033808 (2018).
- [20] V. Ansari, J. M. Donohue, B. Brecht, and C. Silberhorn, *Optica* **5**, 534 (2018).
- [21] I. A. Walmsley and C. Dorrer, *Adv. Opt. Photonics* **1**, 308 (2009).
- [22] U. Keller, *Nature* **424**, 831 (2003).
- [23] D. J. Kane and R. Trebino, *Opt. Lett.* **18**, 823 (1993).
- [24] C. Iaconis and I. A. Walmsley, *Opt. Lett.* **23**, 792 (1998).
- [25] A. I. Lvovsky and M. G. Raymer, *Rev. Mod. Phys.* **81**, 299 (2009).
- [26] A. I. Lvovsky, H. Hansen, T. Aichele, O. Benson, J. Mlynek, and S. Schiller, *Phys. Rev. Lett.* **87**, 050402 (2001).
- [27] T. Aichele, A. I. Lvovsky, and S. Schiller, *Eur. Phys. J. D* **18**, 237 (2002).
- [28] C. Polycarpou, K. N. Cassemiro, G. Venturi, A. Zavatta, and M. Bellini, *Phys. Rev. Lett.* **109**, 053602 (2012).
- [29] O. Morin, C. Fabre, and J. Laurat, *Phys. Rev. Lett.* **111**, 213602 (2013).
- [30] Z. Qin, A. S. Prasad, T. Brannan, A. MacRae, A. Lezama, and A. I. Lvovsky, *Light: Science & Applications* **4**, e298 (2015).
- [31] P. Chen, C. Shu, X. Guo, M. M. T. Loy, and S. Du, *Phys. Rev. Lett.* **114**, 010401 (2015).
- [32] N. Tischler, A. Büse, L. G. Helt, M. L. Juan, N. Piro, J. Ghosh, M. J. Steel, and G. Molina-Terriza, *Physical Review Letters* **115**, 193602 (2015).
- [33] J. Tiedau, V. S. Shchesnovich, D. Mogilevtsev, V. Ansari, G. Harder, T. J. Bartley, N. Korolkova, and C. Silberhorn, *New J. Phys.* **20**, 033003 (2018).
- [34] F. Boitier, A. Godard, N. Dubreuil, P. Delaye, C. Fabre, and E. Rosencher, *Nature Communications* **2**, 425 (2011).
- [35] V. Ansari, G. Harder, M. Allgaier, B. Brecht, and C. Silberhorn, *Phys. Rev. A* **96**, 063817 (2017).
- [36] V. Ansari, J. M. Donohue, M. Allgaier, L. Sansoni, B. Brecht, J. Roslund, N. Treps, G. Harder, and C. Silberhorn, *Phys. Rev. Lett.* **120**, 213601 (2018).
- [37] A. O. C. Davis, V. Thiel, M. Karpiński, and B. J. Smith, *Phys. Rev. Lett.* **121**, 083602 (2018).
- [38] A. O. C. Davis, V. Thiel, and B. J. Smith, *arXiv:1809.03727* (2018).
- [39] J.-P. W. MacLean, J. M. Donohue, and K. J. Resch, *Phys. Rev. Lett.* **120**, 053601 (2018).
- [40] J.-P. W. MacLean, J. M. Donohue, and K. J. Resch, *Phys. Rev. A* **97**, 063826 (2018).
- [41] K. Zielnicki, K. Garay-Palmett, D. Cruz-Delgado, H. Cruz-Ramirez, M. F. O'Boyle, B. Fang, V. O. Lorenz, A. B. U'Ren, and P. G. Kwiat, *Journal of Modern Optics* **65**, 1141 (2018).
- [42] R. W. Gerchberg and W. Saxton, *Optik* **35**, 237 (1972).
- [43] J. R. Fienup, *Appl. Opt.* **52**, 45 (2013).
- [44] Y. Shechtman, Y. C. Eldar, O. Cohen, H. N. Chapman, J. Miao, and M. Segev, *IEEE Signal Processing Magazine* **32**, 87 (2015).
- [45] D. Peri, *Appl. Opt.* **26**, 1782 (1987).
- [46] J. R. Fienup, *Opt. Lett.* **3**, 27 (1978).
- [47] J. R. Fienup, *Appl. Opt.* **21**, 2758 (1982).
- [48] P. J. Mosley, J. S. Lundeen, B. J. Smith, P. Wasylczyk, A. B. U'Ren, C. Silberhorn, and I. A. Walmsley, *Phys. Rev. Lett.* **100**, 133601 (2008).
- [49] S. Mancini, V. Giovannetti, D. Vitali, and P. Tombesi, *Phys. Rev. Lett.* **88**, 120401 (2002).
- [50] Y.-W. Cho, K.-K. Park, J.-C. Lee, and Y.-H. Kim, *Phys. Rev. Lett.* **113**, 063602 (2014).
- [51] M. Guizar-Sicairos and J. R. Fienup, *J. Opt. Soc. Am. A* **29**, 2367 (2012).
- [52] R. Trebino, *Frequency-Resolved Optical Gating: The Measurement of Ultrashort Laser Pulses* (Springer Science & Business Media, 2012).
- [53] W. O. Saxton, *Computer Techniques for Image Processing in Electron Microscopy* (Academic Press, 2013).
- [54] W. H. Press, S. A. Teukolsky, W. T. Vetterling, and B. P. Flannery, *Numerical Recipes 3rd Edition: The Art of Scientific Computing* (Cambridge University Press, 2007).
- [55] D. J. Kane, *IEEE Journal of Quantum Electronics* **35**, 421 (1999).
- [56] E. Treacy, *J. Quantum Electron.* **5**, 454 (1969).
- [57] D. N. Fittinghoff, K. W. DeLong, R. Trebino, and C. L. Ladera, *J. Opt. Soc. Am. B* **12**, 1955 (1995).
- [58] B. A. Korzh, Q.-Y. Zhao, S. Frasca, J. P. Allmaras, T. M. Autry, E. A. Bersin, M. Colangelo, G. M. Crouch, A. E. Dane, T. Gerrits, F. Marsili, G. Moody, E. Ramirez, J. D. Rezac, M. J. Stevens, E. E. Wollman, D. Zhu, P. D. Hale, K. L. Silverman, R. P. Mirin, S. W. Nam, M. D. Shaw, and K. K. Berggren, *arXiv:1804.06839* (2018).
- [59] P. O'Shea, M. Kimmel, X. Gu, and R. Trebino, *Opt. Express* **7**, 342 (2000).
- [60] P. Thibault and A. Menzel, *Nature* **494**, 68 (2013).
- [61] C. Bourassin-Bouchet and M.-E. Couprie, *Nat. Commun.* **6**, 6465 (2015).